Journal of Materials Chemistry B

Accepted Manuscript

ROYAL SOCIETY OF CHEMISTRY

www.rsc.org/materialsB

Graphical Abstract

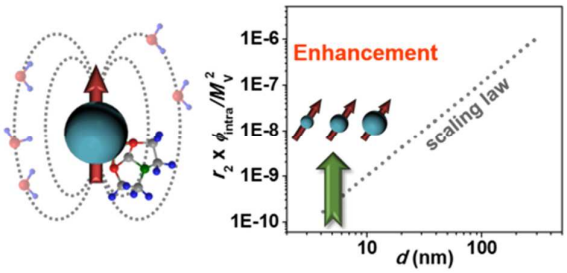

Superparamagnetic Fe_3O_4 nanomaterials with enhanced relaxometric properties were prepared by coprecipitation using alkanolamines with different chelating properties. The alkanolamines promoted these achievements by mastering the surface magnetic properties upon size reduction.

Architectured Design of Superparamagnetic Fe_3O_4 Nanoparticles for Application as MRI Contrast Agents: Mastering Size and Magnetism for Enhanced Relaxivity

Clara Pereira,[a,*] André M. Pereira,[b] Mariana Rocha,[a] Cristina Freire[a] and Carlos F. G. C. Geraldes[c,*]

[a] REQUIMTE/LAQV, Departamento de Química e Bioquímica, Faculdade de Ciências, Universidade do Porto, 4169-007 Porto, Portugal

[b] IFIMUP and IN – Institute of Nanoscience and Nanotechnology, Departamento de Física e Astronomia, Faculdade de Ciências, Universidade do Porto, 4169-007 Porto, Portugal

[c] Departamento de Ciências da Vida, Faculdade de Ciências e Tecnologia, Centro de Neurociências e Biologia Celular and Centro de Química de Coimbra, Universidade de Coimbra, 3000-393 Coimbra, Portugal

***Corresponding authors:**

Dr. Clara Pereira: Tel: +351 220402576; Fax: +351 220402659; e-mail: clara.pereira@fc.up.pt

Dr. Carlos F. G. C. Geraldes: Tel: +351 239853608; Fax: +351 239853601; e-mail: geraldes@ci.uc.pt

Abstract

This work reports the mastered design of novel water-dispersible superparamagnetic iron oxide nanomaterials with enhanced magnetic properties and reduced size. A straightforward cost-effective aqueous coprecipitation route was developed, based on the use of three new coprecipitation agents: the polydentate bases diethanolamine, triethanolamine and triisopropanolamine. Through the selection of these alkanolamines which presented different complexing properties, an improvement of the surface spin order could be achieved upon the reduction of the nanomaterial dimensions (from 8.7 to 3.8 nm) owing to the complexation of the polydentate bases with the subcoordinated iron cations on the particle surface. In particular, the alkanolamine with the highest chelating ability (triethanolamine) led to the nanomaterial with the smallest size and the thinnest magnetic "dead" layer.

In order to evaluate the importance of the dual control of size and magnetism, the relaxometric properties of the nanomaterials were investigated, whereby maximum values of transverse relaxivity r_2 of 300.30 and 253.92 mM^{-1} s^{-1} at 25 and 37 ºC, respectively (at 20 MHz) were achieved, making these nanomaterials potential T_2-weighted MRI contrast agents. Moreover, these values were significantly higher than those reported for commercial T_2 contrast agents and other iron oxides with identical dimensions. Hence, we were able to demonstrate that the r_2 enhancement cannot only be achieved by an increase of particle/cluster size, but also through the precise control of the surface magnetic properties while constraining the nanomaterial dimensions. These achievements open new perspectives on the mastered design of magnetic nanoprobes, overcoming the limitations related with the deleterious effect of size reduction.

Keywords: iron oxides, magnetic nanoparticles, coprecipitation, magnetic resonance imaging, contrast agent

1. Introduction

Iron oxide nanoparticles are a class of magnetic nanomaterials that has been revolutionizing a myriad of scientific and technological areas such as biomedicine,[1] catalysis,[2] and water splitting.[3] They occupy a pivotal position as high-performance probes for theranostic applications owing to their unique magnetic properties, reduced toxicity, biocompatibility and tunable surface chemistry.[1,4,5]

In the diagnosis field, superparamagnetic (SPM) magnetite (Fe_3O_4) and maghemite (γ-Fe_2O_3) nanoparticles have been among the prime choices as contrast agents (CAs) in magnetic resonance imaging (MRI).[6,7] These nanoprobes typically act as negative CAs by shortening the transverse relaxation time (T_2) of water protons, leading to a negative contrast enhancement (dark signal on MR images against a bright background).[8,9] Additionally, when compared with paramagnetic CAs, they can enhance proton relaxation at lower dosages, improving the MRI sensitivity.

Several types of SPM iron oxide nanoparticles (SPIONs) and ultra-small SPIONs (USPIONs, overall size: <40 nm) have already been commercialized or are under clinical trials.[1,6,7,10,11] They consist of SPM single cores or multicore nanoclusters coated with a biocompatible shell of dextran (Feridex®/Endorem®, Combidex®/Sinerem®), carboxydextran (Resovist), etc.

The most common and straightforward route to prepare this type of agents has been the aqueous coprecipitation of Fe(II) and Fe(III) salts, under alkaline conditions, in the presence or absence of a hydrophilic capping/coating agent.[12,13] The versatility of this process lies on its cost-effectiveness, eco-sustainability (mild reaction conditions, non-toxic reagents) and scalability.[12–14] Additionally, it offers the possibility of directly obtaining water-dispersible nanomaterials without requiring further treatments, which is of prime importance for biomedical applications. However, the control over the particle

size distribution and overall magnetization is still challenging, which are key parameters to enhance the relaxometric properties of the CA.

Several strategies have been developed to achieve more efficient T_2 CAs. Most are based on the thermal decomposition of metal complex precursors in high-temperature organic solvents in the presence of surfactants.[12–14] Cheon *et al.* prepared hydrophobic Fe_3O_4 magnetic nanoparticles (MNPs) with different size by thermal decomposition followed by a ligand-exchange step with 2,3-dimercaptosuccinic acid (DMSA) to make them hydrophylic.[15,16] By gradually increasing the particle size from 4 to 12 nm, the saturation magnetization (M_S) significantly increased from 25 to 102 emu g^{-1}, which led to a progressive T_2 contrast enhancement at 1.5 T, with the transverse relaxivity values (r_2) increasing from 78 to 218 mM^{-1} s^{-1}. Other authors reported similar size-dependent effects to enhance the T_2 contrast efficiency of surfactant-capped SPIONs prepared by thermal decomposition, arising from the improvement of the magnetic properties.[17–20] More recently, the change of the particle morphology from spherical to cubic,[21] octapod,[22] nanoplatelets,[23] etc., was proposed as a promising route to enhance the T_2 contrast of iron oxides. A distinct strategy to enhance the MRI contrast of T_2-weighted magnetic nanoprobes is based on the chemical substitution of Fe(II) by other divalent 3*d*-metal cations.[9,10,18] Cheon and co-authors reported that, for a set of 12 nm nanoferrites (MFe_2O_4, M = Mn(II), Fe(II), Co(II), Ni(II)), the highest r_2 value of 358 mM^{-1} s^{-1} at 1.5 T was achieved for $MnFe_2O_4$, which was simultaneously the nanoferrite with the highest M_S (110 emu g^{-1}).[16] The r_2 values could be further enhanced by partial substitution of Fe(II) and Mn(II) by Zn(II), reaching 687 and 860 mM^{-1} s^{-1} at 4.7 T for 15 nm $Zn_{0.4}Fe_{0.6}Fe_2O_4$ and $Zn_{0.4}Mn_{0.6}Fe_2O_4$, respectively.[24]

Although the MNPs prepared by thermal decomposition exhibited promising contrast efficiency, this process requires the use of high reaction temperatures,

hazardous solvents and reagents.[12–14] Furthermore, an additional ligand exchange step is required to make the as-synthesized MNPs water-dispersible,[10,14] hampering their commercialization.

The polyol method has recently emerged as an alternative one-step route to synthesize water-dispersible MNPs with controlled size.[12,13] In this process, the MNP synthesis is performed in a high-boiling polyol solvent, which also acts as reducing agent, particle growth restrainer and hydrophilic capping agent. For instance, Meade *et al.* prepared SPM Fe_3O_4 nanoparticles with sizes ranging from 3 to 6 nm.[25,26] The highest r_2 value of 119 mM^{-1} s^{-1} at 1.41 T was achieved for the 6 nm MNPs. Nevertheless, the r_2 values obtained through this route are often lower than those achieved by thermal decomposition.

In this context, the quest for novel eco-friendly one-pot routes for the rational design of high-performance water-dispersible T_2 CAs combining small particle size, superparamagnetism and enhanced M_S continues to be a thriving milestone. The combination of these key features is of crucial importance to improve the MRI signal sensitivity at lower CA dosage and, simultaneously, prevent the nanoparticles' aggregation in solution. A major concern continues to be the preservation of the magnetic properties when scaling down the nanomaterial dimensions, since this often leads to a reduction of the M_S due to an increase of the surface spin disorder, resulting in a decrease of the T_2 contrast efficiency.[18]

In view of these challenges, this work reports the fabrication of a new generation of water-dispersible SPM Fe_3O_4 nanoparticles combining reduced size with enhanced M_S, surface spin order and relaxivity, by a one-pot aqueous coprecipitation process. The novelty of this route lies on the use of three new coprecipitation agents with different chelating properties – the alkanolamines diethanolamine (DEA), triethanolamine (TEA)

and triisopropanolamine (TIPA). The alkanolamines play a multiple role during the Fe_3O_4 synthesis, both as alkaline agents and, more importantly, as complexing agents, restraining the particle size and mastering the spin arrangement at the surface. Recently, we reported the importance of alkanolamines for the synthesis of nanoferrites (MFe_2O_4, M = Mn(II), Fe(II), Co(II)) with controlled size and magnetic properties but for two distinct bases isopropanolamine and diisopropanolamine.[27] Nevertheless, no relation between the achieved improvements and the structural differences of both bases could be established.

In the present work, through the selection of three polydentate alkanolamines with different structural features, we endeavor to study the influence of the alkanolamine structure on the physicochemical properties of the resulting iron oxides, with the ultimate goal to master their magnetic properties and surface spin order upon the reduction of the particle size. Furthermore, and more importantly, the relaxometric properties of the SPM nanoparticles are evaluated in order to unveil the role of the enhanced magnetic features and small size on their CA efficiency. This work fosters the advances on the tailored design of high-performance CAs through a one-pot cost-effective and scalable route.

2. Experimental section

2.1 Materials and reagents

Iron(II) chloride tetrahydrate, iron(III) chloride hexahydrate and hydrochloric acid (37%), all of analytical grade, were purchased from Merck. DEA (≥99.0%) and TIPA (95%) were supplied by Aldrich and TEA (≥98.5%) was purchased from Fluka. Absolute ethanol and acetone (analytical grade) were obtained from Fisher Chemical.

Ultrapure water (Millipore, specific resistivity 18 MΩ cm) was used throughout the experiments. All reagents were used without further purification.

2.2 Preparation of iron oxide magnetic nanoparticles

The Fe_xO_y magnetic nanomaterials were synthesized by aqueous coprecipitation, using three new coprecipitation agents – DEA, TEA and TIPA. Firstly, 10 mmol of $FeCl_2.4H_2O$ and 20 mmol of $FeCl_3.6H_2O$ were dissolved in 25 cm^3 of deoxygenated 0.5 M HCl solution and heated to 70 ºC. The resulting solution was quickly mixed with 250 cm^3 of a deoxygenated 3.0 M aqueous solution of DEA, TEA or TIPA at 100 ºC with vigorous mechanical stirring under an argon atmosphere. A black precipitate formed immediately. The reaction mixture was stirred at 100 ºC for 2 h under inert atmosphere and then cooled to room temperature. Afterwards, the resulting black precipitate was magnetically separated and washed with deoxygenated water several times until neutral pH. Finally, the precipitate was redispersed in deoxygenated water and stored under inert atmosphere. The resulting ferrofluids remained stable over extended periods of time. The iron oxide samples prepared with DEA, TEA and TIPA will be labeled as Fe_DEA, Fe_TEA and Fe_TIPA, respectively.

2.3 Physicochemical characterization

X-ray diffraction (XRD) measurements were performed at room temperature over the 2θ range of 20−80°, at the Departamento de Química and CQ-VR, Universidade de Trás-os-Montes e Alto Douro (UTAD), Portugal, with a PW 3040/60 X'Pert Pro Röntgen diffractometer using Cu Kα radiation (λ = 1.5406 Å) and the Bragg−Brentano $\theta/2\theta$ configuration. The system includes the ultrafast PW3015/20 X'Celerator detector

and a secondary monochromator. The Rietveld refinements and simulations of Bragg reflections of the XRD patterns were performed with FULLPROF software.

Transmission electron microscopy (TEM), high-resolution TEM (HRTEM) and selected area electron diffraction (SAED) were performed at the Departamento de Engenharia Cerâmica e do Vidro, Universidade de Aveiro, Portugal, with a Hitachi H-9000NA microscope operating at an accelerating voltage of 300 kV. The samples were dispersed in high-purity ethanol under sonication, followed by the immersion of a holey carbon-coated 400 mesh copper grid (Agar) in the resulting suspension and subsequent air-drying. A slight aggregation of the nanoparticles was observed due to magnetic interactions with the electron beam. The average particle sizes and size distributions were calculated from the diameters of more than 150 particles randomly selected from the TEM micrographs.

Fourier transform infrared (FTIR) spectra of the MNPs were recorded with a Jasco FT/IR-460 Plus spectrophotometer in the 400−4000 cm^{-1} range, at room temperature, using a resolution of 4 cm^{-1} and 32 scans. The spectra of the samples were obtained in KBr pellets (Aldrich, FTIR spectroscopy grade) containing 1 wt% of MNPs.

The iron concentration of the colloidal dispersions analyzed by dynamic light scattering (DLS), zeta potential and relaxometry studies were determined by atomic absorption spectroscopy using a Philips PU 9200X device with a hollow cathode lamp (S & J Juniper & Co).

DLS and zeta potential studies were performed at 25 ºC, using a Malvern Zetasizer NanoZS compact scattering spectrometer with a 4.0 mW He–Ne laser (633 nm wavelength) at a scattering angle of 173º. The aqueous colloidal dispersions were analyzed in a polystyrene cell or in a standard capillary electrophoresis cell, for size distribution and zeta potential measurements, respectively. The hydrodynamic diameters

and zeta potential of the samples were determined using Malvern Dispersion Technology Software 7.01. The Smoluchowsky equation was used for the calculation of the zeta potential values. All measurements were repeated five times for each sample to verify the reproducibility of the results.

Thermogravimetric analysis (TGA) was carried out at LSRE/LCM, Departamento de Engenharia Química, Faculdade de Engenharia da Universidade do Porto, Portugal, on a Netzsch STA 409 PC/PG thermobalance in the temperature range of 50–700 °C at a heating rate of 10 °C min^{-1} under a nitrogen flow (50 mL min^{-1}).

The magnetic properties of the dried MNPs were studied using a commercial Quantum Design superconducting quantum interference device (SQUID) magnetometer. The magnetization as a function of applied magnetic field ($M(H)$) was performed at 300 and 5 K for a maximum applied magnetic field of 30 kOe. Temperature-dependent zero-field-cooled (ZFC) and field-cooled (FC) measurements were performed over the range of 5−370 K with an applied magnetic field of 100 Oe.

The longitudinal (T_1) and transverse (T_2) proton relaxation times of the aqueous dispersions of the iron oxide samples with different iron concentrations were measured at 25 and 37 ºC by magnetic resonance relaxometry on a Bruker Minispec mq20 relaxometer operating at a magnetic field of 0.47 T, corresponding to a proton Larmor frequency of 20 MHz. T_1 values were measured using an inversion recovery pulse sequence, while T_2 values were measured using a Carr–Purcell–Meiboom–Gill (CPMG) pulse sequence and varying the time interval between two consecutive refocusing pulses in the train of 180° applied pulses. All the experimental values were corrected taking into account the diamagnetic contribution of water. The corresponding relaxivity values, r_1 and r_2, were calculated through the least-squares curve fitting of the inverse relaxation time $1/T_i$ (i = 1,2) (s^{-1}) *vs.* the iron concentration (mM Fe).

3. Results and discussion

3.1 Structural, morphological and chemical properties

The iron oxide nanomaterials were characterized by XRD and TEM in order to provide information about their crystalline structure, composition, morphology and particle size. The X-ray diffractograms of all samples (Figure 1) exhibit the typical Bragg reflections of ferrites at 30.1º, 35.4º, 43.1º, 53.4º, 56.9º, 62.5º and 74.0º (obtained from the Rietveld refinement), which correspond to the (220), (311), (400), (422), (511), (440) and (533) planes, respectively. These features indicate that the nanomaterials are crystalline and present a cubic spinel structure (space group *Fd3m*). The peak broadening is due to the small size of the crystalline domains.[28]

Figure 1

In order to identify the nature of the iron oxides, the diffractograms were fitted using the Rietveld refinement (inset of Figure 1), considering a single phase. For all samples, the resulting lattice parameter *a* of the cubic unit cell is ~8.370 Å, which is an intermediate value between those of bulk Fe_3O_4 (8.396 Å, JCPDS card No. 19-0629) and γ-Fe_2O_3 (8.346 Å, JCPDS card No. 39-1346), indicating the presence of both types of iron oxide phases. In this context, a second Rietveld refinement was performed considering the existence of both phases, which allowed estimating the amount of Fe_3O_4 and γ-Fe_2O_3. In all samples, the main crystalline phase is Fe_3O_4 (>75%) with a small fraction of γ-Fe_2O_3 probably due to surface oxidation phenomena arising from their nanometer size.[29] These results are in accordance with the lattice parameter estimated considering a single phase (value closer to that of bulk Fe_3O_4) as well as with the black color of the nanomaterials which is characteristic of magnetite.

The average particle size, d_{XRD}, and internal microstrain, η, were determined using the Williamson-Hall relation:[27]

$$\beta_{total} = \beta_{size} + \beta_{strain} = \frac{K\lambda}{d_{XRD}\cos\theta} + 4\eta\tan\theta \quad (1)$$

where β_{total} is the full width at half-maximum of the XRD peak, K is the Debye-Scherrer constant (~0.94 for spherical nanoparticles), λ is the incident X-ray wavelength and θ is the diffraction angle. For all samples the internal microstrain is negligible ($\eta < 10^{-3}$), indicating that the MNPs are essentially strain-free.[27]

The estimated d_{XRD} values (Table 1) decrease in the order of Fe_TIPA (9.0 nm) > Fe_DEA (5.9 nm) > Fe_TEA (4.8 nm), indicating that the particle dimensions can be tuned by changing the base type. Furthermore, the nanomaterials present smaller sizes than those prepared by coprecipitation with common alkaline agents reported in the literature (e.g. NaOH, NH_3, tetramethylammonium hydroxide, etc.);[30,31] when compared with iron oxides prepared with other alkanolamines, isopropanolamine and diisopropanolamine,[27] their dimensions are comparable or lower as in the case of Fe_TEA.

Table 1

Complementary information concerning the nanomaterials' structure, morphology and particle size/size distribution was obtained by TEM coupled with selected area electron diffraction (SAED) and HRTEM.

Figure 2

The TEM micrographs (Figure 2) reveal that all the iron oxide nanomaterials exhibit a quasi-spherical shape, with log-normal size distributions (Figure S2 in the

Supplementary Information). In the HRTEM images of the nanomaterials (presented as insets in Figure 2) can be observed uniform lattice fringes with a *d*-spacing of 0.25 nm, which corresponds to the (311) Bragg reflection of magnetite. These results confirm the crystalline nature of the samples with a highly ordered atomic arrangement. Additionally, a thin layer surrounding the nanoparticles is detected which is due to the presence of the organic base at their surface.

The SAED patterns of the samples (presented in Figure S1 in the Supplementary Information) exhibit the characteristic rings/spots that can be indexed to the lattice planes of a cubic spinel lattice,[28,32] corroborating the XRD and HRTEM results.

Concerning the nanomaterials' dimensions estimated by TEM, the samples present different average particle size (d_{TEM} values in Table 1), which decreases in the order of Fe_TIPA (8.7 nm) > Fe_DEA (5.3 nm) > Fe_TEA (3.8 nm), paralleling the size reduction trend obtained by XRD (Table 1). Additionally, for all the nanomaterials, the d_{TEM} values are of the same order of magnitude as the average crystallite sizes estimated by XRD, indicating that the iron oxide nanoparticles can be considered as single crystals.[33]

In this context, both XRD and TEM techniques suggest that the base type used in the nanomaterials' synthesis has a dominant role on the control of their dimensions. DEA, TEA and TIPA belong to the family of polydentate alkanolamine bases, differing in the number of hydroxyl groups and/or existence of methyl substituents in the alkanol chains: DEA contains a secondary amine and two hydroxyl groups (Figure 3A); on the other hand, both TEA and TIPA contain a tertiary amine and three hydroxyl groups (Figures 3B and 3C, respectively), with TIPA presenting methyl substituents in the carbon atoms adjacent to the OH groups.

Figure 3

In the literature, it has been stated that these polydentate alkanolamines can act as chelating ligands towards 3*d* transition metal cations through their hydroxyl and amine groups (multidentate ligands), forming complexes in aqueous solution.[34–36] DEA generally acts as a NO_2-tridentate ligand,[37] whereas both TEA and TIPA have four potential binding sites (NO_3) to coordinate to the metal cation center, behaving as NO_2-tri- or NO_3-tetradentate ligands.[37,38] Since all the alkanolamine solutions present moderate and comparable alkalinities, albeit being slightly higher for DEA, the reduction of the size ongoing from Fe_TIPA to Fe_TEA is probably governed by their different chelating ability. In this context and taking into account previous works,[34,39–41] we propose that the alkanolamines coordinate with Fe(II) and Fe(III) cations through their hydroxyl and amine groups. Since the reaction is carried out at 100 ºC, the Fe-alkanolamine complexes hydrolyze to the corresponding intermediate iron hydroxide species which are then converted into the final iron oxides.[40,41]

Our results also suggest that among the three alkanolamines, TEA is the most efficient agent for the particle size reduction. When comparing both ethanolamines (DEA *vs.* TEA), TEA has a higher chelating ability than DEA since it is able to coordinate to the iron cations through up to four coordinating atoms. This stronger coordination is probably responsible for the enhanced control over the nucleation and particle growth rates during the coprecipitation process, leading to the particles with the smallest size. In fact, in the last years the complexing properties of TEA have been reported in the literature in the synthesis of ferromagnetic micrometer sized Fe_3O_4 crystals,[42,43] 44 nm size Fe_3O_4 nanoclusters,[44] and in the formation of 3–4 μm Fe_3O_4 peony-like structures.[45] More recently, TEA was used as ligand to iron precursors in the synthesis of Fe_3O_4 nanoparticles, but the reported procedure still required using NaOH

base (NaOH:TEA molar ratio = 36:6) and a Fe(II)/Fe(III) ratio of 1.33, resulting in particles with sizes above 7.8 nm.[46]

On the other hand, since DEA only contains two hydroxyl groups instead of three, the stability enhancement of the corresponding Fe-DEA complexes[34] will be smaller, leading to a weaker coordination and thus explaining the larger size of Fe_DEA nanoparticles.

Finally, although TIPA is a close analog of TEA, it presents three methyl groups in the carbon atoms adjacent to the coordinating OH groups, which leads to steric hindrance to iron cations coordination. This will cause a weaker chelating effect, and consequently give rise to less control over the nucleation and growth processes yielding particles with the largest size among the three prepared nanomaterials. These results are further supported by FTIR, TGA and SQUID magnetometry (see below).

The FTIR spectra of all the nanomaterials (Figure 4) present a strong band at 580 cm^{-1} ascribed to Fe–O stretching vibrations of the magnetite framework,[27,47] with a shoulder around 625 cm^{-1} due to the slight surface oxidation,[48] sustaining the iron oxide identification by XRD. A second Fe–O stretching vibration band is observed in the low frequency side but cannot be resolved since it is below the detection limit of our FTIR equipment (<400 cm^{-1}). Besides these features, several bands/peaks are detected over the whole wavenumber range which correspond to the fingerprint vibrational modes of the alkanolamine bases: C–H asymmetric and symmetric stretching (2974–2860 cm^{-1}),[38,49] C–H bending (1456–1320 cm^{-1}),[49–51] C–N and C–O stretching vibrations (Fe_TEA: at 1098 and 1069 cm^{-1}, respectively; Fe_DEA: vibrational modes coupled at ~1067 cm^{-1}; Fe_TIPA: ~1135 cm^{-1}, coupled).[38,50–53] The broad band around ~3405 cm^{-1} and the band at ~1623 cm^{-1} are respectively assigned to O–H stretching and bending vibrations of surface hydroxyl groups, alkanolamines and physisorbed water.[49,53] In the

case of Fe_DEA, the N–H stretching and bending vibration modes of DEA could not be detected since they are masked by the bands related with O–H stretching and bending vibrations.[49,50]

Figure 4

Hence, these features confirm the presence of the bases at the nanomaterial surface. It is also noteworthy that the intensity of the FTIR bands associated with the alkanolamines increases in the order of Fe_TIPA < Fe_DEA < Fe_TEA, indicating that Fe_TEA contains the highest amount of base. Additionally, for all the three nanomaterials, the bands related with C–N and C–O stretching vibrations are shifted to higher wavenumbers when compared to those of the neat bases,[50–52] especially in the case of Fe_TEA (1072 and 1038 cm^{-1} for the pure TEA base *vs.* 1098 and 1069 cm^{-1} for Fe_TEA). These trends thus confirm that the alkanolamines are coordinated to the particles' surface through their N and O atoms, with TEA presenting the strongest capping properties, sustaining our proposed mechanism.

The alkanolamine bases are not only responsible for the tuning of the nanomaterials' dimensions but also for their high colloidal stability in aqueous medium as can be confirmed visually (inset of Figure S3 in the Supplementary Information with photograph of Fe_TEA colloidal dispersion and corresponding TEM image) and by DLS and zeta potential studies. The average hydrodynamic diameter values (d_{DLS}), which represent the overall particle size, follow the same trend observed by TEM and XRD (Table 1), albeit being higher due to the presence of the chelating agents at the nanomaterial surface and/or existence of some particle clustering. Furthermore, the hydrodynamic particle size distribution curves are unimodal (Figure S3 in the Supplementary Information for Fe_TEA) with small polydispersity index (PDI) values

(below 0.2, Table 1). No signals of flocculation or changes of the hydrodynamic particle size were detected for at least six months storage (see hydrodynamic size distribution of Fe_TEA aqueous dispersion after 6 months in Figure S3 in the Supplementary Information), which confirms the high stability of the colloidal dispersions in water. Futhermore, the hydrodynamic size distributions preserve the unimodal behavior.

For all the three sample dispersions, the zeta potential values are higher than +30 mV (threshold value for colloidal stability),[54] indicating that the nanomaterials present a positive surface charge at neutral pH imparted by the hydrophilic alkanolamine molecules coordinated to their surface.

The amount of alkanolamine adsorbed on the nanomaterials' surface was quantified by TGA. The thermograms of the three samples (Figure S4 in the Supplementary Information) reveal the existence of three main weight loss steps: (i) the first weight loss occurs in the range of 50–160 ºC and is related with the removal of physisorbed water and surface hydroxyl groups; (ii) the second and most significant weight loss occurs in the range of 160–335 ºC for Fe_DEA, 160–375 ºC for Fe_TEA and 160–420 ºC for Fe_TIPA, being assigned to the depletion of physisorbed alkanolamines; and (iii) the third weight loss occurs up to 665 ºC (Fe_DEA: 650 ºC, Fe_TEA: 670 ºC Fe_TIPA: 607 ºC) being ascribed to the thermal decomposition of alkanolamine molecules chemically bound to the particles' surface, which is more prominent in the case of Fe_TEA.[55,56]

When comparing the three nanomaterials, the total weight loss increases in the order of Fe_TIPA < Fe_DEA < Fe_TEA (Table 1), confirming that the nanomaterial with the smallest particle size (Fe_TEA) contains the highest amount of organic species on its surface, in accordance with FTIR results. This tendency can be justified by the progressive decrease of the nanomaterials' dimensions, and consequently, by the

increase of the surface area to volume ratio.[55] It is also noteworthy that the total depletion of TEA in Fe_TEA ends at a higher temperature, which is probably related with its stronger coordinating properties relative to those of DEA and TIPA, since ligands that are more strongly bound desorb at higher temperatures.[56]

3.2 Magnetic properties

A detailed study on the magnetization (*M*) of the iron oxide nanoparticles as a function of temperature (*T*) and applied magnetic field (*H*) was performed by SQUID magnetometry. Concerning the temperature dependence measurements, the resulting ZFC-FC curves provided information concerning the nature of the magnetic state of the nanomaterials at room temperature (Figure 5).

Figure 5

From Figure 5, it can be observed that for all the nanomaterials there is a clear overlap of the ZFC and FC curves at 300 K, which is an evident feature of a SPM state at room temperature. Consequently, in order to estimate the temperature that separates the unblocked from the blocked state, the difference between ZFC and FC curves was determined numerically, and subsequently, the corresponding derivative was plotted as a function of temperature (not shown). The obtained blocking temperature (T_B) values were approximately 127.9, 36.7 and 16.9 K for Fe_TIPA, Fe_DEA and Fe_TEA, respectively (Table 2). It outcomes that the T_B values correlate well with the particle size tendency observed by TEM and XRD, being in accordance with the Stoner−Wohlfarth relation:[57]

$$K_{\text{eff}} d^3 = \frac{150 k_B T_B}{\pi} \quad (2)$$

where K_{eff} is the effective anisotropy constant, d is d_{TEM} and k_B is the Boltzmann constant.

The K_{eff} values were determined using the same relation, and are summarized in Table 2. By plotting K_{eff} as a function of $1/d_{TEM}$, a linear relation is obtained (see inset of Figure 5), showing that the magnetic anisotropy of all nanomaterials follows the relation given by:[57]

$$K_{eff} = K_{bulk} + 6K_{surf}/d_{TEM} \quad (3)$$

From the linear fitting, the bulk anisotropy (K_{bulk}) and surface anisotropy (K_{surf}) values were extracted, being ~69 kJ m^{-3} and ~84 kJ m^{-2}, respectively. The obtained K_{bulk}, although being of the same order of magnitude as that reported in the literature (12 kJ m^{-3}),[57] is 6 times larger indicating that the MNPs' inner structure has a strong magnetocrystalline anisotropy. Furthermore, from Figure 5, a plateau can be observed in the FC curves at low temperatures, which is characteristic of the presence of dipolar interactions.[58] This effect is more patent in the Fe_TIPA sample followed by Fe_DEA and Fe_TEA.

Table 2

The confirmation of the SPM state at room temperature of all nanomaterials was also unveiled through the *M vs. H* curves at 300 K (Figure 6A), where negligible coercive field values were obtained. This feature is of crucial importance for biomedical applications in order to prevent the existence of interparticle aggregation in the dispersion arising from magnetic interactions. On the other hand, the *M vs. H* curves at 5 K exhibit magnetic hysteresis (Figure 6B), with coercive field (H_C) values of 370, 327 and 140 Oe for Fe_TIPA, Fe_DEA and Fe_TEA, respectively (Table 2). These results

reveal that the MNPs are blocked at 5 K, *i.e.* the interaction between the MNPs is higher than thermal fluctuations.

Figure 6

Another parameter extracted from the $M(H)$ curves at 5 and 300 K (Figure 6) is the saturation magnetization (M_S), which is of crucial importance to evaluate differences in the magnetic properties of the three nanomaterials. In particular, for technological applications, the M_S values near room temperature deserve special attention to evaluate the nanomaterial performance in the common operating temperatures. The M_S values at 300 K increase in the order of Fe_DEA (57.1 emu g^{-1}) < Fe_TEA (60.1 emu g^{-1}) < Fe_TIPA (65.1 emu g^{-1}), revealing that the saturation magnetization remains practically constant regardless of the nanomaterial dimensions. These magnetic results are in general better than those reported in the literature for Fe_3O_4 MNPs of identical size synthesized by the coprecipitation method with other bases or by other methods reported in the literature.[27,29,30,59]

From the $M(H)$ curves at 5 K (Figure 6B), the M_S values were extrapolated to 0 K (M_{S0}) in order to estimate the magnitude of the disordered spins at the nanomaterial surface, expressed by the thickness of the "dead" layer (D_L), given by:[58]

$$M_{S0} = M_S^{bulk}\left(\frac{D_{TEM}/2 - D_L}{D_{TEM}/2}\right)^3 \quad (4)$$

where the M_{S0} values were normalized taking into account the magnetic component of the samples determined by TGA, in order to obtain an accurate estimation of the D_L.

The D_L values decrease in the order of Fe_TIPA > Fe_DEA > Fe_TEA (Table 2), revealing that the nanomaterial with the smallest size, *i.e.*, prepared with TEA, presents the lowest degree of surface spin canting disorder, while that prepared with TIPA

(largest size) possesses the highest degree. These results can thus be related with the chelating properties of the three bases: among the three bases, TEA is responsible not only for the most significant particle size constrain but also for the highest degree of surface spin order.

In order to assess the importance of the tuned magnetic properties upon size reduction, the relaxometric properties of the Fe_3O_4 nanomaterials were investigated.

3.3 Relaxometric properties

For each iron oxide sample, the longitudinal and transverse water proton relaxation times (T_1 and T_2, respectively) of the aqueous dispersions at different iron concentrations were measured, both at 25 ºC and at 37 ºC, at a magnetic field of 0.47 T (Larmor frequency of 20 MHz). A linear dependence between the inverse proton relaxation times (*i.e.* the water proton relaxation rates) and the iron concentration is obtained for the three nanomaterials and for both $1/T_1$ and $1/T_2$ (see representative plots at 37 ºC in Figure 7), in accordance with the following equation:[12]

$$\frac{1}{T_{\mathrm{i,obs}}} = \frac{1}{T_{i,0}} + r_i[\mathrm{Fe}] \qquad (5)$$

where $1/T_{\mathrm{i,obs}}$ (i = 1, 2) is the inverse relaxation time measured experimentally in the presence of the magnetic nanomaterial, $1/T_{\mathrm{i},0}$ is the inverse relaxation time of pure water in the absence of the contrast agent, [Fe] is the iron concentration in the contrast agent and r_{i} is the longitudinal (i = 1) or transverse (i = 2) relaxivity (*i.e.* proton relaxation rate enhancement per mM Fe cations concentration).

Figure 7

The r_1 and r_2 values at 25 and 37 ºC, which provide information concerning the contrast agent efficiency, were extracted from the slopes of the linear regressions and are presented in Table 2.

Since the ability of the presently studied magnetic CAs to increase the rate of nuclear magnetic resonance relaxation of surrounding protons is mostly based on their effect on r_2, we will start by discussing those results. The r_2 values of Fe_TIPA, Fe_DEA and Fe_TEA dispersions at 25 ºC are 300.30, 277.53 and 275.76 mM^{-1} s^{-1}, respectively, slightly decreasing to 253.92, 230.52 and 204.91 mM^{-1} s^{-1} at 37 ºC, revealing their potential as T_2 CAs. Among the three nanomaterials, Fe_TIPA exhibits the highest r_2 values, probably due to its larger particle size[12] since the M_S values of all samples are very similar.

It is noteworthy that, when compared with commercially available T_2 CAs and other iron oxides with identical particle size reported in the literature (Table 3),[11,23,60–67] the three nanomaterials present significantly higher r_2 values (at 0.47 T and 37 ºC). In particular, a 34–378% enhancement of r_2 is achieved when compared with the best commercially available T_2-type CAs (Resovist® and Sinerem®, respectively, Table 3).[11] More remarkably, these r_2 values are comparable to or larger than those recently reported at 0.47 T for iron oxides and transition metal ferrites with larger particle size,[23,62,63,66,67] non-spherical morphology[23,64] and/or core-shell structures (Table 3).[65] Nevertheless, when compared with magnetic CAs combining larger particle size and higher M_S (Table 3), as for example with Fe@$MnFe_2O_4$ (16 nm),[65] the r_2 values at room temperature reported herein are slightly lower, but of the same order of magnitude.

Table 3

We also compared our r_2 data obtained at 0.47 T with the r_2 values of some of the most promising nanosystems reported in the literature at higher magnetic fields (Table 3).[9] The r_2 values at room temperature for magnetic Fe_3O_4 nanocubes (FION),[68] manganese(II) ferrite nanoparticles (MnMEIO)[16] and core-shell $Fe@Fe_xO_y$ nanoparticles[69,70] fall in the 312–358 mM^{-1} s^{-1} range, being comparable to the value obtained for Fe_TIPA at that temperature. An exceptionally high transverse relaxivity of 860 mM^{-1} s^{-1} was reported for a mixed zinc(II)-manganese(II) nanoferrite ($Zn_{0.4}Mn_{0.6}Fe_2O_4$).[24] Nevertheless, all these MNPs are substantially larger (12–58 nm) than those studied in this work and have quite high M_S values, in particular the zinc(II)-manganese(II) nanoferrite system. A qualitative comparison of our r_2 values at 0.47 T with those measured for such systems at 1.5, 4.5 and 9.4 T is possible because for SPM iron oxide nanoparticles the saturation magnetization is almost reached at 0.47 T, being expected an almost constant r_2 beyond that applied magnetic field B_0.[71] Therefore, regardless of their crystal size, the r_2 values of USPIONs should show no magnetic field dependence above 0.47 T (20 MHz),[60,61] as the saturation magnetization is practically reached at that B_0 value.

The origin of the r_2 enhancement observed for our set of nanomaterials was unveiled by delving into their physicochemical properties. As it is well known, r_2 strongly depends, among other parameters, on the morphology, particle size and magnetic properties of the CAs,[9,12,18,72] following different relaxation regimes. In the case of small SPM nanoparticles or coated with a thin fully hydrated shell, their interaction with the water protons can be theoretically described by the quantum-mechanical outer sphere theory, following a motional averaging regime (MAR).[8,9,12] In the MAR regime ($\Delta\omega\tau_D < 1$), the relation between r_2, the nanomaterial dimensions and magnetic properties is given by:[73]

$$r_2 = \frac{4\gamma^2 \mu_0^2 v_{mat} M_V^2 d^2}{405 D} \quad (6)$$

where γ is the proton gyromagnetic factor (2.67513×10^8 rad s^{-1} T^{-1}), μ_0 is the vacuum magnetic permeability ($4\pi \times 10^{-7}$ T m A^{-1}), v_{mat} is the nanomaterial molar volume ($v_{mat} = \frac{M_{MFe_2O_4}}{3\rho_{MFe_2O_4}}$ for spinel-type transition metal ferrites, with M being the molar mass and ρ the mass density), M_V is the total saturation magnetization divided by the particle volume (in A m^{-1}), d is the particle diameter of the iron oxide core obtained by TEM, D is the diffusion constant of water molecules, $\Delta\omega$ is the difference in angular frequencies between the local field experienced by a proton at the equatorial line of the cluster surface and in the bulk ($\Delta\omega = \gamma\mu_0 M_V / 3$) and τ_D is the translational diffusion correlation time of the protons in the magnetic field inhomogeneities generated by the particles ($\tau_D = d^2 / 4D$).

According to this equation, for iron oxide samples in the MAR regime, r_2 presents a quadratic dependence on both d and M_V. To disclose if the transverse relaxometry results obtained in this work follow the aforementioned relation, the r_2 values of the three samples were plotted as a function of $M_V^2 d^2$ (Figure 8). Linear relations were obtained both at 25 and 37 ºC, confirming that the relaxometric properties of our samples follow the MAR regime.

Figure 8

Recently, Sandre *et al.* compared the transverse relaxation properties at 37 ºC and at 0.47 or 1.41 T for different magnetic nanomaterials (4–300 nm) which followed the MAR model, both prepared by the authors and by other research groups, namely single MNPs, iron oxide clusters, core-shell silica-coated MNPs and magnetic vesicles.[73] The

main purpose was to assess the existence of a universal law that fitted all the results, by plotting $r_2 \times \phi_{intra}$ values normalized by M_V^2 as a function of d (where ϕ_{intra} is the intra-aggregate volume fraction of magnetic component in clusters and hybrids). The authors were able to establish a universal experimental curve, which confirmed the reliability of the theoretical MRI relaxation models.

To unveil if the results obtained in the present work follow that universal experimental curve, they were included in the $r_2 \times \phi_{intra} / M_V^2$ *versus* d plot from reference 73 (Figure 9). As can be observed from Figure 9, only Fe_TIPA fairly follows the universal scaling law proposed by the authors. However, ongoing from Fe_TIPA to Fe_TEA, a progressive deviation to the linear scaling tendency is observed. This is especially highlighted for the sample with the smallest size, Fe_TEA, which presents a $r_2 \times \phi_{intra} / M_V^2$ value significantly higher than those reported/predicted for other nanosystems with similar dimensions d (highlighted by the blue arrow). Deviations to the proposed r_2 universal scaling law have also been reported for nanosystems presenting faceted or nanoplate morphology as a consequence of their non-spherical shape which is not considered in this model.[23,60]

Figure 9

On the other hand, for our set of samples, the normalized r_2 values remain practically constant regardless of d, in spite of the progressive reduction of the particle size ongoing from Fe_TIPA to Fe_TEA. Therefore, the similarity between the normalized r_2 values suggests that the magnetic properties of the nanomaterials are playing a dominant role. In the literature it has been stated that, in general, the reduction of the particle size leads to a decrease of r_2, since typically the size reduction is accompanied by an increase of the nanomaterial surface spin canting, originating a

lower saturation magnetization.[15,74] However, in this work, the normalized relaxometric properties are preserved upon the reduction of the particle size. This can be justified taking into account the magnetic properties of the as-prepared iron oxides: ongoing from Fe_TIPA to Fe_TEA there is a progressive decrease of the thickness of the magnetic dead layer. This leads to a gradual improvement of the magnetic spin arrangement at the surface of the nanomaterial, with Fe_TEA presenting the most ordered surface. In this context, although the size is reduced, the magnetic properties are preserved giving rise to comparable normalized r_2 values.

This is a main breakthrough for the architectured design of efficient T_2 contrast agents since through the selection of the alkanolamine coprecipitation agent, the MNPs' size can be tuned to the required dimensions while preserving their MRI contrast efficiency. In this context, the r_2 enhancement cannot only be achieved by an increase of the particle size or through particle clustering,[9,10,72] but also by tailoring the magnetic surface properties while preserving the small particle size.

Another important parameter which is typically used to evaluate a contrast agent efficiency is the r_2/r_1 ratio. High r_2/r_1 ratios ($\geq$2) result in T_2-dominated contrast and lower ratios (<1–2) lead to T_1-dominated contrast.[75] For the three nanomaterials, the r_2/r_1 ratio is above 10 which confirms their potential as new T_2-type MRI CAs. This results from their low r_1 values at 0.47 T, which are practically constant and independent of the particle size. It is known that the longitudinal relaxivity r_1 of these SPM nanoparticles depends on two relaxation mechanisms:[12] a) the Néel relaxation, due to the fluctuations of the orientation of the superparamagnetic crystal magnetic moment relative to the external magnetic field B_0, with a Néel relaxation time τ_N; and b) the outer-sphere Curie relaxation mechanism, arising from the diffusion of the water protons into the inhomogeneous non-fluctuating local magnetic field created by the

mean crystal magnetic moment aligned with B_0, with a translational diffusion correlation time τ_D. The proportion of each contribution is fully dependent on the crystal size and applied magnetic field B_0, which requires a thorough study of the dependence of r_1 on a wide range of magnetic fields that is beyond the scope of the present work.

4. Conclusions

Novel superparamagnetic Fe_3O_4 nanoparticles with high aqueous colloidal stability, reduced dimensions and, simultaneously, high saturation magnetization were prepared by a one-step aqueous coprecipitation route. Through the use of new polydentate alkanolamine bases, we were able to master the magnetic spin ordering at the surface, giving rise to the preservation of the superparamagnetic state while reducing the particle size. The origin of these features was related with the distinct chemical structure of the three alkanolamine bases, namely the number of hydroxyl groups and/or existence of methyl substituents in the alkanol chains.

These remarkable achievements were responsible for the strong enhancement of the T_2 contrast efficiency, with the r_2 values surpassing those reported for state-of-the-art magnetic contrast agents with comparable dimensions.

These improvements sustain the importance of designing novel synthesis strategies to engineer the nanomaterial properties when scaling-down the particle dimensions. We believe that the work reported herein is a stepping stone to understand the joint role of size and magnetism on the enhanced T_2 contrast efficiency of iron oxide MRI nanoprobes. Furthermore, the potentialities of these magnetic nanomaterials go beyond their application in MRI, namely in magnetic hyperthermia, targeted drug delivery, eco-sustainable catalysis and magnetic sensing.

Acknowledgments

This work was funded by Fundação para a Ciência e a Tecnologia (FCT) and FEDER through grants no. PEst-C/EQB/LA0006/2013, FCOMP-01-0124-FEDER-037285 and FEDER/POCTIn0155/94. The authors also acknowledge Operation NORTE-07-0124-FEDER-000067 – NANOCHEMISTRY, NORTE-070124-FEDER-000070 – MULTIFUNCTIONAL NANOMATERIALS and the Portuguese National NMR Network (RNRMN) supported by FCT. The authors thank Prof. J. L. Figueiredo and Prof. M. F. R. Pereira from LSRE/LCM for access to TGA equipment, Prof. J. P. Araújo from IFIMUP-IN for access to SQUID magnetometer and Prof. P. Tavares and MSc. L. Fernandes from UTAD for XRD measurements. M. R. thanks FCT for a grant.

References

1 L. H. Reddy, J. L. Arias, J. Nicolas and P. Couvreur, *Chem. Rev.*, 2012, **112**, 5818.

2 D. Wang and D. Astruc, *Chem. Rev.*, 2014, **114**, 6949.

3 S. C. Warren, K. Voïtchovsky, H. Dotan, C. M. Leroy, M. Cornuz, F. Stellacci, C. Hébert, A. Rothschild and M. Grätzel, *Nat. Mater.*, 2013, **12**, 842.

4 L. Zhang, W.-F. Dong and H.-B. Sun, *Nanoscale*, 2013, **5**, 7664.

5 D. Yoo, J.-H. Lee, T.-H. Shin and J. Cheon, *Acc. Chem. Res.*, 2011, **44**, 863.

6 M. Mahmoudi, H. Hosseinkhani, M. Hosseinkhani, S. Boutry, A. Simchi, W. S. Journeay, K. Subramani and S. Laurent, *Chem. Rev.*, 2011, **111**, 253.

7 F. Hu and Y. S. Zhao, *Nanoscale*, 2012, **4**, 6235.

8 A. J. L. Villaraza, A. Bumb and M. W. Brechbiel, *Chem. Rev.*, 2010, **110**, 2921.

9 N. Lee and T. Hyeon, *Chem. Soc. Rev.*, 2012, **41**, 2575.

10 L. Li, W. Jiang, K. Luo, H. Song, F. Lan, Y. Wu and Z. Gu, *Theranostics*, 2013, **3**, 595.

11 C. F. G. C. Geraldes and S. Laurent, *Contrast Media Mol Imag.*, 2009, **4**, 1.

12 S. Laurent, D. Forge, M. Port, A. Roch, C. Robic, L. V. Elst and R. N. Muller, *Chem. Rev.*, 2008, **108**, 2064.

13 M. Colombo, S. Carregal-Romero, M. F. Casula, L. Gutiérrez, M. P. Morales, I. B. Böhm, J. T. Heverhagen, D. Prosperi and W. J. Parak, *Chem. Soc. Rev.*, 2012, **41**, 4306.

14 J. Gallo, N. J. Long and E. O. Aboagye, *Chem. Soc. Rev.*, 2013, **42**, 7816.

15 Y.-W. Jun, Y.-M. Huh, J.-S. Choi, J.-H. Lee, H.-T. Song, S. Kim, S. Yoon, K.-S. Kim, J.-S. Shin, J.-S. Suh and J. Cheon, *J. Am. Chem. Soc.*, 2005, **127**, 5732.

16 J.-H. Lee, Y.-M. Huh, Y.-W. Jun, J.-W. Seo, J.-T. Jang, H.-T. Song, S. Kim, E.-J. Cho, H.-G. Yoon, J.-S. Suh and J. Cheon, *Nat. Med.*, 2007, **13**, 95.

17 H. Duan, M. Kuang, X. Wang, Y. A. Wang, H. Mao and S. Nie, *J. Phys. Chem. C*, 2008, **112**, 8127.

18 Y.-W. Jun, J.-H. Lee and J. Cheon, *Angew. Chem., Int. Ed.*, 2008, **47**, 5122.

19 A. G. Roca, S. Veintemillas-Verdaguer, M. Port, C. Robic, C. J. Serna and M. P. Morales, *J. Phys. Chem. B*, 2009, **113**, 7033.

20 J. Huang, L. Bu, J. Xie, K. Chen, Z. Cheng, X. Li and X. Chen, *ACS Nano*, 2010, **4**, 7151.

21 N. Lee, Y. Choi, Y. Lee, M. Park, W. K. Moon, S. H. Choi and T. Hyeon, *Nano Lett.*, 2012, **12**, 3127.

22 Z. Zhao, Z. Zhou, J. Bao, Z. Wang, J. Hu, X. Chi, K. Ni, R. Wang, X. Chen, Z. Chen and J. Gao, *Nat. Commun.*, 2013, **4**, 2266.

23 Z. Zhou, Z. Zhao, H. Zhang, Z. Wang, X. Chen, R. Wang, Z. Chen and J. Gao, *ACS Nano*, 2014, **8**, 7976.

24 J.-T. Jang, H. Nah, J.-H. Lee, S. H. Moon, M. G. Kim and J. Cheon, *Angew. Chem., Int. Ed.*, 2009, **48**, 1234.

25 F. Hu, K. W. MacRenaris, E. A. Waters, T. Liang, E. A. Schultz-Sikma, A. L. Eckermann and T. J. Meade, *J. Phys. Chem. C*, 2009, **113**, 20855.

26 F. Hu, H. M. Joshi, V. P. Dravid and T. J. Meade, *Nanoscale*, 2010, **2**, 1884.

27 C. Pereira, A. M. Pereira, C. Fernandes, M. Rocha, R. Mendes, M. P. Fernández-García, A. Guedes, P. B. Tavares, J.-M. Grenèche, J. P. Araújo and C. Freire, *Chem. Mater.*, 2012, **24**, 1496.

28 M. Das, D. Mishra, P. Dhak, S. Gupta, T. K. Maiti, A. Basak and P. Pramanik, *Small*, 2009, **5**, 2883.

29 A. Demortière, P. Panissod, B. P. Pichon, G. Pourroy, D. Guillon, B. Donnio and S. Bégin-Colin, *Nanoscale*, 2011, **3**, 225.

30 R. L. Rebodos and P. J. Vikesland, *Langmuir*, 2010, **26**, 16745.

31 V. Ström, R. T. Olsson and K. V. Rao, *J. Mater. Chem.*, 2010, **20**, 4168.

32 V. Yathindranath, Z. Sun, M. Worden, L. J. Donald, J. A. Thliveris, D. W. Miller and T. Hegmann, *Langmuir*, 2013, **29**, 10850.

33 D. Caruntu, Y. Remond, N. H. Chou, M.-J. Jun, G. Caruntu, J. He, G. Goloverda, C. O'Connor and V. Kolesnichenko, *Inorg. Chem.*, 2002, **41**, 6137.

34 F. M. Al-Sogair, B. P. Operschall, A. Sigel, H. Sigel, J. Schnabl and R. K. O. Sigel, *Chem. Rev.*, 2011, **111**, 4964.

35 L. G. Sillén and A. E. Martell, *Stability Constants of Metal-Ion Complexes*, Supplement No. 1, Special Publication No. 25, The Chemical Society, London, 1971.

36 T. Bechtold, S. Mohr, W. Schrott, N. Grund and W. Hiebsch, *US Pat.*, 6814763 B2, 2004.

37 A. Singh and R. C. Mehrotra, *Coord. Chem. Rev.*, 2004, **248**, 101.

38 A. M. Kirillov, Y. Y. Karabach, M. Haukka, M. F. C. G. da Silva, J. Sanchiz, M. N. Kopylovich and A. J. L. Pombeiro, *Inorg. Chem.*, 2008, **47**, 162.

39 D. Caruntu, G. Caruntu, Y. Chen, C. J. O'Connor, G. Goloverda and V. L. Kolesnichenko, *Chem. Mater.*, 2004, **16**, 5527.

40 L. Wang, H. Ji, S. Wang, L. Kong, X. Jiang and G. Yang, *Nanoscale*, 2013, **5**, 3793.

41 M. Chen, Y. N. Kim, C. Li and S. O. Cho, *J. Phys. Chem. C*, 2008, **112**, 6710.

42 J. Liang, L. Li, M. Luo and Y. Wang, *Cryst. Res. Technol.*, 2011, **46**, 95.

43 R. S. Sapieszko and E. Matijević, *J. Colloid lnterface Sci.*, 1980, **74**, 405.

44 D. Maity, P. Chandrasekharan, P. Pradhan, K.-H. Chuang, J.-M. Xue, S.-S. Feng and J. Ding, *J. Mater. Chem.*, 2011, **21**, 14717.

45 J. Wang, T. Xia, C. Wu, J. Feng, F. Meng, Z. Shi and J. Meng, *RSC Adv.*, 2012, **2**, 4220.

46 T. Xia, J. Wang, C. Wu, F. Meng, Z. Shi, J. Lian, J. Feng and J. Meng, *CrystEngComm*, 2012, **14**, 5741.

47 R. M. Cornell and U. Schwertmann, *The Iron Oxides: Structure, Properties, Reactions, Occurrence and Uses*, Wiley-VCH, Weinheim, Germany, 1996.

48 W. Baaziz, B. P. Pichon, S. Fleutot, Y. Liu, C. Lefevre, J.-M. Greneche, M. Toumi, T. Mhiri and S. Begin-Colin, *J. Phys. Chem. C*, 2014, **118**, 3795.

49 M. A. Melo Jr. and C. Airoldi, *Dalton Trans.*, 2010, **39**, 10217.

50 G. Richner and G. Puxty, *Ind. Eng. Chem. Res.*, 2012, **51**, 14317.

51 S. C. Rustagi and G. N. Rao, *J. Inorg. Nucl. Chem.*, 1974, **36**, 1889.

52 T. Ban, Y. Ohya and Y. Takahashi, *J. Sol-Gel Sci. Technol.*, 2003, **27**, 363.

53 Y.-S. Fu, X.-W. Du, S. A. Kulinich, J.-S. Qiu, W.-J. Qin, R. Li, J. Sun and J. Liu, *J. Am. Chem. Soc.*, 2007, **129**, 16029.

54 R. Xu, *Particle Characterization: Light Scattering Methods*, Particle Technology Series, Vol. 13, ed. B. Scarlett, Kluwer Academic Publishers, Dordrecht, Nederland, 2002.

55 J.-H. Huang, H. J. Parab, R.-S. Liu, T.-C. Lai, M. Hsiao, C.-H. Chen, H.-S. Sheu, J.-M. Chen, D.-P. Tsai and Y.-K. Hwu, *J. Phys. Chem. C*, 2008, **112**, 15684.

56 R. de Palma, S. Peeters, M. J. Van Bael, H. Van den Rul, K. Bonroy, W. Laureyn, J. Mullens, G. Borghs and G. Maes, *Chem. Mater.*, 2007, **19**, 1821.

57 J. M. D. Coey, *Magnetism and magnetic materials*, Cambridge University Press, Cambridge, United Kingdom, 2009.

58 A. M. Pereira, C. Pereira, A. S. Silva, D. S. Schmool, C. Freire, J.-M. Grenèche and J. P. Araújo, *J. Appl. Phys.*, 2011, **109**, 114319.

59 L. Xiao, J. Li, D. F. Brougham, E. K. Fox, N. Feliu, A. Bushmelev, A. Schmidt, N. Mertens, F. Kiessling, M. Valldor, B. Fadeel and S. Mathur, *ACS Nano*, 2011, **5**, 6315.

60 E. D. Smolensky, H.-Y. E. Park, Y. Zhou, G. A. Rolla, M. Marjańska, M. Botta and V. C. Pierre, *J. Mater. Chem. B*, 2013, **1**, 2818.

61 L. Lartigue, C. Innocenti, T. Kalaivani, A. Awwad, M. M. S. Duque, Y. Guari, J. Larionova, C. Guérin, J.-L. G. Montero, V. Barragan-Montero, P. Arosio, A. Lascialfari, D. Guatteschi and C. Sangregorio, *J. Am. Chem. Soc.*, 2011, **133**, 10459.

62 G. Huang, H. Li, J. Chen, Z. Zhao, L. Yang, X. Chi, Z. Chen, X. Wang and J. Gao, *Nanoscale*, 2014, **6**, 10404.

63 M. Hatakeyama, H. Kishi, Y. Kita, K. Imai, K. Nishio, S. Karasawa, Y. Masaike, S. Sakamoto, A. Sandhu, A. Tanimoto, T. Gomi, E. Kohda, M. Abe and H. Handa, *J. Mater. Chem.*, 2011, **21**, 5959.

64 T. Shen, R. Weissleder, M. Papisov, A. Bogdanov Jr. and T. J. Brady, *Magn. Reson. Med.*, 1993, **29**, 599.

65 T.-J. Yoon, H. Lee, H. Shao and R. Weissleder, *Angew. Chem., Int. Ed.*, 2011, **50**, 4663.

66 S. Tong, S. Hou, Z. Zheng, J. Zhou and G. Bao, *Nano Lett.*, 2010, **10**, 4607.

67 C. Chouly, D. Pouliquen, I. Lucet, J. J. Jeune and P. Jallet, *J. Microencapsul.*, 1996, **13**, 245.

68 N. Lee, H. Kim, S. H. Choi, M. Park, D. Kim, H.-C. Kim, Y. Choi, S. Lin, B. H. Kim, H. S. Jung, H. Kim, K. S. Park, W. K. Moon and T. Hyeon, *Proc. Nat. Acad. Sci. U.S.A.*, 2011, **108**, 2662.

69 H. Lee, T.-J. Yoon and R. Weissleder, *Angew. Chem., Int. Ed.*, 2009, **48**, 5657.

70 S. Cheong, P. Ferguson, K. W. Feindel, I. F. Hermans, P. T. Callaghan, C. Meyer, A. Slocombe, C.-H. Su, F.-Y. Cheng, C.-S. Yeh, B. Ingham, M. F. Toney and R. D. Tilley, *Angew. Chem., Int. Ed.*, 2011, **50**, 4206.

71 Y. Gossuin, P. Gillis, A. Hocq, Q. L. Vuong and A. Roch, *Wiley Interdiscip. Rev.: Nanomed. Nanobiotechnol.*, 2009, **1**, 299.

72 H. B. Na, I. C. Song and T. Hyeon, *Adv. Mater.*, 2009, **21**, 2133.

73 Q. L. Vuong, J.-F. Berret, J. Fresnais, Y. Gossuin and O. Sandre, *Adv. Healthcare Mater.*, 2012, **1**, 502.

74 J. Cheon and J.-H. Lee, *Acc. Chem. Res.*, 2008, **41**, 1630.

75 P. Caravan, J. J. Ellison, T. J. McMurray and R. B. Lauffer, *Chem. Rev.*, 1999, **99**, 2293.

Table 1. Average particle size determined by XRD, TEM and DLS, zeta potential values and total weight loss estimated by TGA

Nanomaterial	Average particle size			Hydrodynamic diameter		Zeta potential (mV)	Total weight loss[f] (%)
	d_{XRD}[a] (nm)	d_{TEM}[b] (nm)	σ_{TEM}[c]	d_{DLS}[d] (nm)	PDI[e]		
Fe_TIPA	9.0	8.7	0.1	39.0 ± 0.4	0.19	38.8 ± 0.3	7.3
Fe_DEA	5.9	5.3	0.2	35.0 ± 0.3	0.17	37.8 ± 0.4	10.9
Fe_TEA	4.8	3.8	0.2	30.3 ± 0.3	0.18	37.2 ± 0.8	14.8

[a] Average particle size estimated by XRD.
[b] Average particle size estimated by TEM, assuming a log-normal size distribution.
[c] Standard deviation.
[d] Average hydrodynamic diameter estimated by DLS.
[e] Polydispersion index.
[f] Determined by TGA under N_2 atmosphere.

Table 2. Magnetic and relaxometric parameters of the iron oxide MNPs

Sample	Magnetic properties						Relaxometric Properties					
	$M_S^{300\ K}$ (emu g^{-1})	$M_S^{5\ K}$ (emu g^{-1})	$H_C^{5\ K}$ (Oe)	T_B (K)	$10^3\ K_{eff}$ (J m^{-3})	D_L (nm)	$r_1^{25\ °C}$ ($mM^{-1}\ s^{-1}$)	$r_2^{25\ °C}$ ($mM^{-1}\ s^{-1}$)	r_2/r_1 25 °C	$r_1^{37\ °C}$ ($mM^{-1}\ s^{-1}$)	$r_2^{37\ °C}$ ($mM^{-1}\ s^{-1}$)	r_2/r_1 37 °C
Fe_TIPA	65.1	74.9	370	127.9	128.0	0.12	28.70	300.30	10.46	19.48	253.92	13.03
Fe_DEA	57.1	68.0	327	36.7	162.4	0.10	21.08	277.53	13.17	17.33	230.52	13.30
Fe_TEA	60.1	75.5	140	16.9	202.8	0.01	23.01	275.76	11.98	18.27	204.91	11.22

Table 3. Comparison of the structural, magnetic and relaxometric properties of the as-synthesized MNPs with those of typical T_2-type CAs reported in the literature at 0.47 T and at higher magnetic fields

Name	Magnetic core	Capping/ Coating agent	d_{TEM} (nm)	d_{DLS} (nm)	M_S (emu g^{-1})	T (°C)	r_1 (mM^{-1} s^{-1})	r_2 (mM^{-1} s^{-1})	r_2/r_1	B_o (T)	Ref.
IO-26	Spherical Fe_3O_4 nanoparticles	DMSA[a]	26		39.8	32	16.49 ± 2.87	167.89 ± 2.36	10.4	0.47	23
IO-21			21		48.7		11.73 ± 0.24	232.16 ± 4.91	19.7		
IO-16			16		65.1		7.67 ± 1.05	118.83 ± 4.07	15.5		
IO-10			10		54.8		3.74 ± 0.19	59.38 ± 5.34	15.9		
IO-9			9		49.8		4.55 ± 0.14	53.34 ± 2.13	11.7		
IO-5			5		36.5		6.02 ± 1.29	39.63 ± 1.93	6.58		
IO-3			3		6.5		2.41 ± 0.11	13.12 ± 1.79	5.44		
IOP-8.8	Fe_3O_4 nanoplates	DMSA[a]	34 (8.8 thick)		74.1	32	38.11 ± 1.04	311.88 ± 7.47	8.18	0.47	23
IOP-4.8			28 (4.8 thick)		57.6		43.18 ± 3.33	182.2 ± 7.73	4.22		
IOP-2.8			22 (2.8 thick)		34.5		14.36 ± 1.24	78.63 ± 6.41	5.47		
MnIO 12 nm	Mn-doped iron oxide	Tartrate	12.20 ± 0.86	22.28 ± 1.11	71.0	[b]	38.2 ± 1.3	280.8 ± 2.9	7.4	0.47	62
MnIO 9 nm			8.98 ± 0.81	16.79 ± 0.04	60.3		32.1 ± 1.1	205.5 ± 1.2	6.4		
MnIO 7 nm			7.04 ± 0.58	13.21 ± 0.43	52.1		27.2 ± 1.2	146.5 ± 1.9	5.4		
MnIO 5 nm			5.06 ± 0.52	10.49 ± 0.16	39.7		18.0 ± 1.1	45.9 ± 1.1	2.6		
IO 12 nm	Iron oxide	Tartrate	12		60	[b]	14.2	135.2	9.5	0.47	62
IO 7 nm			7				7.7	73.7	9.6		
IO 5 nm			5				4.3	23.0	5.3		
20 nm citrate-MNPs	Fe_3O_4	Citrate	20.7 ± 1.3	20.0 ± 6.2	~55	40	46.5	168.1	3.61	0.47	63
8 nm citrate-MNPs			8.5 ± 0.8	7.6 ± 3.6	45		28.8	54.4	1.89		
4 nm citrate-MNPs			4.6 ± 0.5	4.2 ± 2.8	35		10.5	18.3	1.74		
MION[c]	Hexagonal Fe_3O_4	Dextran	4.6 ± 1.2	20 ± 4	68	37	16.5	34.8	2.1	0.47	64
Fe@FeO	Core-shell Fe@FeO	DMSA[a]	16		92	27	17	188	11.1	0.47	65
Fe@Fe_3O_4	Core-shell Fe@Fe_3O_4		16		142		9	260	28.9		
Fe@$CoFe_2O_4$	Core-shell Fe@$CoFe_2O_4$		16		133		3	243	81.0		
Fe@$MnFe_2O_4$	Core-shell Fe@$MnFe_2O_4$		16		149		11	356	32.4		

[a] DMSA – 2,3-dimercaptosuccinic acid; DSPE-mPEG1000 – 1,2-distearoyl-*sn*-glycero-3-phosphoethanolamine-*N*-[methoxy(polyethylene glycol)] copolymer with molecular weight of 1000 Da; DSPE-mPEG2000 – 1,2-distearoyl-*sn*-glycero-3-phosphoethanolamine-*N*-[methoxy(polyethylene glycol)] copolymer with molecular weight of 2000 Da.
[b] Not specified.
[c] MION – monocrystalline iron oxide nanoparticles; FION – Ferromagnetic iron oxide nanocubes.
[d] Room temperature.

Table 3 (cont.). Comparison of the structural, magnetic and relaxometric properties of the as-synthesized MNPs with those of typical T_2-type CAs reported in the literature at 0.47 T and at higher magnetic fields

Name	Magnetic core	Capping/ Coating agent	d_{TEM} (nm)	d_{DLS} (nm)	M_S (emu g^{-1})	T (°C)	r_1 (mM^{-1} s^{-1})	r_2 (mM^{-1} s^{-1})	r_2/r_1	B_o (T)	Ref.
SPIO-14	Fe_3O_4	DSPE-mPEG1000[a]	13.8 ± 2.2	28.6 ± 0.4		40		385 ± 39		0.47	66
SPIO-5			4.8 ± 0.9	14.8 ± 1.2				130 ± 5			
MD5	Fe_3O_4	Dextran	20–25	90.6 ± 25		37	39	320	8.2	0.47	67
MD4			15–20	75.4 ± 21			44	242	5.5		
MD3			10–15	59 ± 15			44	185	4.2		
MD2			6–8	46.2 ± 10			42	95	2.2		
MD1			2–4	33 ± 9			43	72	1.7		
Sinerem®, Combidex®	Non-stoichiometric magnetite	Dextran	4.3–4.9	~50		37	22.7	53.1	2.3	0.47	11
Endorem™, Feridex®	Non-stoichiometric magnetite	Dextran	4.3–4.8	200		37	24	107	4.5	0.47	11
Resovist	Fe_3O_4/γ-Fe_2O_3	Carboxydextran	4.2	62		37	20	190	9.5	0.47	11
Fe_TIPA	Fe_3O_4	TIPA	8.7	39.0 ± 0.4	65.1	37	19.48	253.92	13.03	0.47	This work
Fe_DEA		DEA	5.3	35.0 ± 0.3	57.1		17.33	230.52	13.30		
Fe_TEA		TEA	3.8	30.3 ± 0.3	60.1		18.27	204.91	11.22		
FION[c]	Fe_3O_4 nanocubes	DSPE - mPEG2000[a]	57.8 ± 9.9		132.1	[b]		324		1.5	68
MnMEIO	$MnFe_2O_4$	DMSA[a]	12		110	RT[d]		358		1.5	16
$Zn_{0.4}Mn_{0.6}Fe_2O_4$	$Zn_{0.4}Mn_{0.6}Fe_2O_4$	DMSA[a]	15		175	RT[d]		860		4.5	24
Cannonball Fe@Fe_xO_y	Core-shell Fe@Fe_xO_y	DMSA[a]	16		139	[b]		312		1.5	69
Fe@Fe_xO_y	α-Fe@Fe_xO_y	DMSA[a]	16 ± 1.5		140–150	RT[d]		324		9.4	70

[a] DMSA – 2,3-dimercaptosuccinic acid; DSPE-mPEG1000 – 1,2-distearoyl-*sn*-glycero-3-phosphoethanolamine-*N*-[methoxy(polyethylene glycol)] copolymer with molecular weight of 1000 Da; DSPE-mPEG2000 – 1,2-distearoyl-*sn*-glycero-3-phosphoethanolamine-*N*-[methoxy(polyethylene glycol)] copolymer with molecular weight of 2000 Da.
[b] Not specified.
[c] MION – monocrystalline iron oxide nanoparticles; FION – Ferromagnetic iron oxide nanocubes.
[d] Room temperature.

Captions to Figures

Figure 1. X-ray diffractograms of the iron oxide nanomaterials. Inset: Rietveld refinement of the X-ray diffractogram of Fe_TIPA nanomaterial. The black line represents the Rietveld refinement and the blue line represents the difference between the experimental data and the fit obtained by Rietveld refinement. The Bragg reflections are indicated by green bars (top bars: Fe_3O_4; bottom bars: γ-Fe_2O_3).

Figure 2. TEM and HRTEM micrographs (inset) of (A) Fe_TIPA, (B) Fe_DEA and (C) Fe_TEA nanomaterials.

Figure 3. Chemical structure of the polydentate bases: (A) DEA, (B) TEA and (C) TIPA.

Figure 4. FTIR spectra of the iron oxide nanomaterials, highlighting the characteristic vibration bands of the iron oxides and alkanolamines. Abbreviations: ν, stretching, δ, bending.

Figure 5. Temperature dependence of the magnetization over the temperature range of 5−370 K with H = 100 Oe in the ZFC and FC regimes for Fe_TIPA, Fe_DEA and Fe_TEA nanomaterials. Inset: K_{eff} as a function of $1/d_{TEM}$.

Figure 6. $M(H)$ loops between -30 kOe and 30 kOe for Fe_TIPA, Fe_DEA and Fe_TEA nanomaterials at (A) 300 K and (B) at 5 K; inset: magnified $M(H)$ curves near the coercive field.

Figure 7. Plots of $1/T_2$ *vs.* Fe concentration for Fe_TIPA, Fe_DEA and Fe_TEA at 37 ºC and corresponding linear regressions.

Figure 8. Linear regressions of r_2 of the three samples *vs.* $M_V^2 d^2$ at 25 and 37 ºC (note: the M_V^2 values were calculated using the density of bulk magnetite,[47] 5180 kg m^{-3}).

Figure 9. Relation between $r_2 \times \phi_{intra} / M_V^2$ and d for iron oxide-based samples in the MAR regime at 37 ºC plotted in reference 73 (which includes the respective data references) and from the samples reported in this work. The arrow highlights the enhancement of the normalized $r_2 \times \phi_{intra} / M_V^2$ achieved for the three nanomaterials Fe_TIPA, Fe_DEA and Fe_TEA when compared with previously reported samples with similar size.

Figure 1

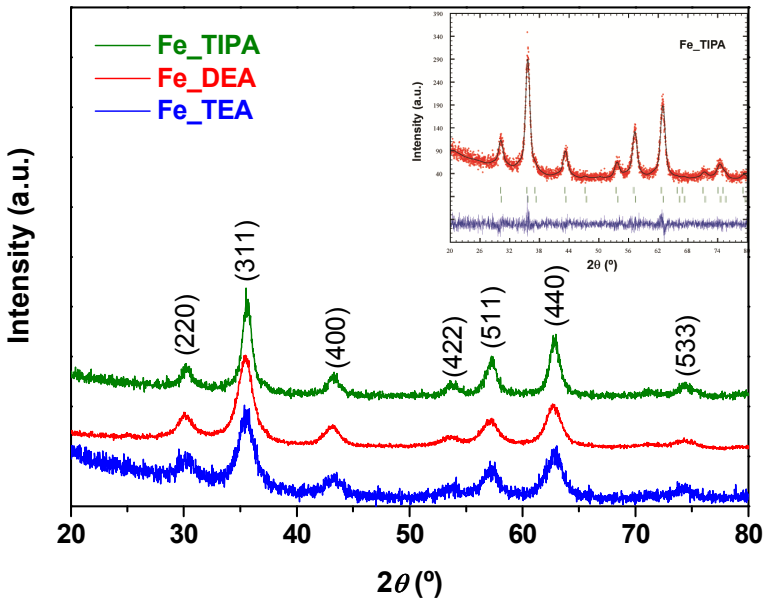

Figure 2

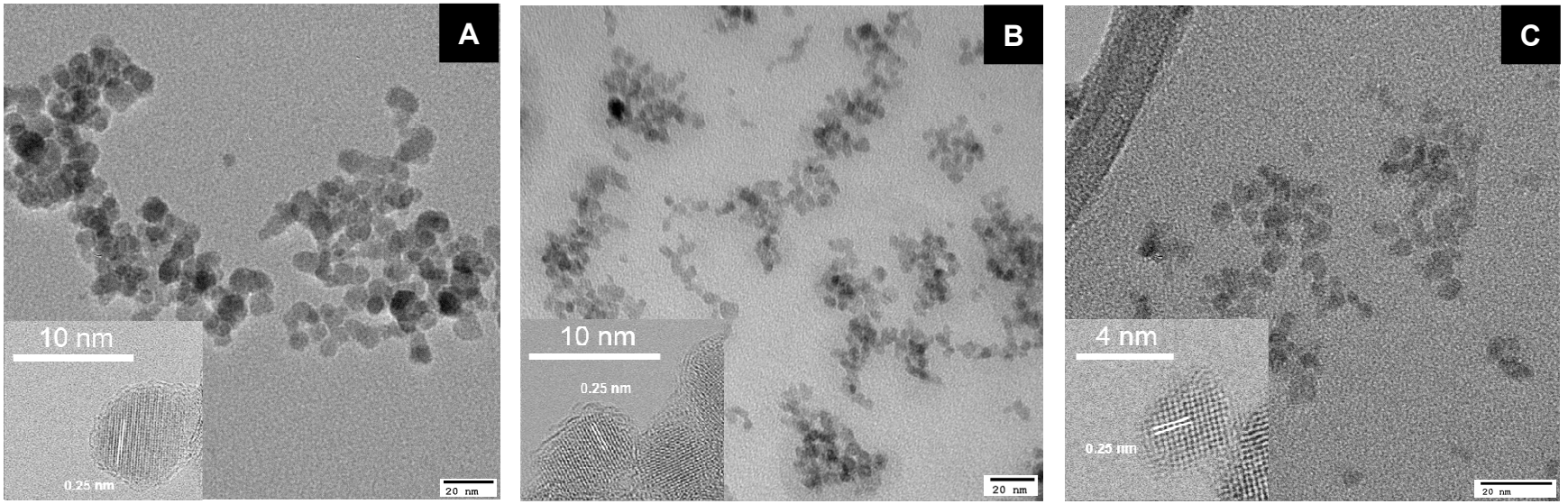

Figure 3

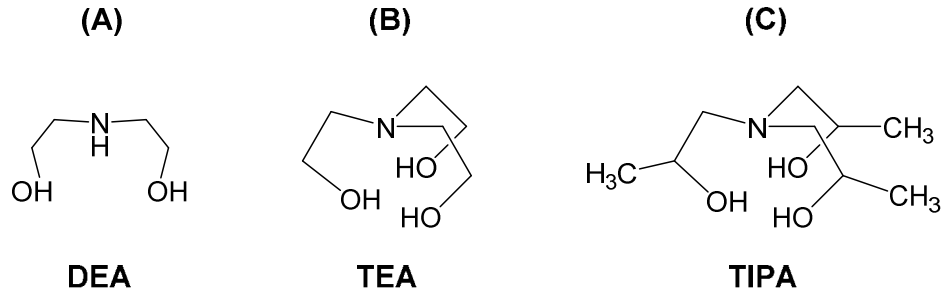

DEA TEA TIPA

Figure 4

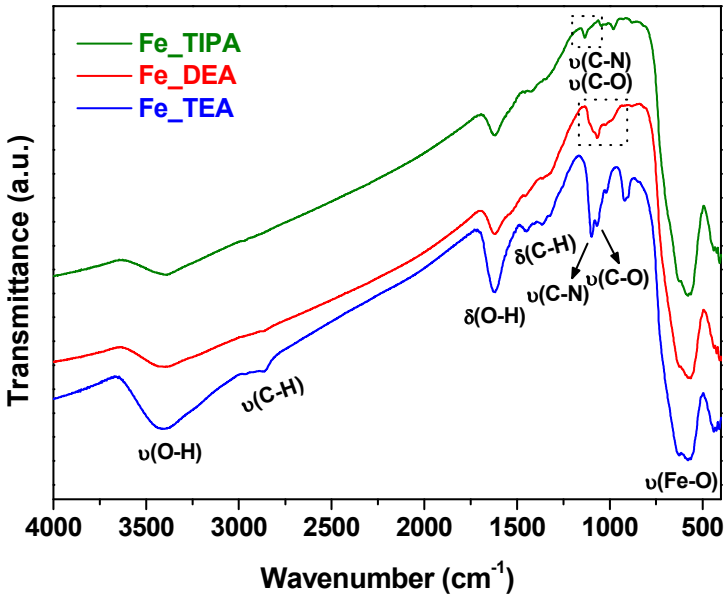

Figure 5

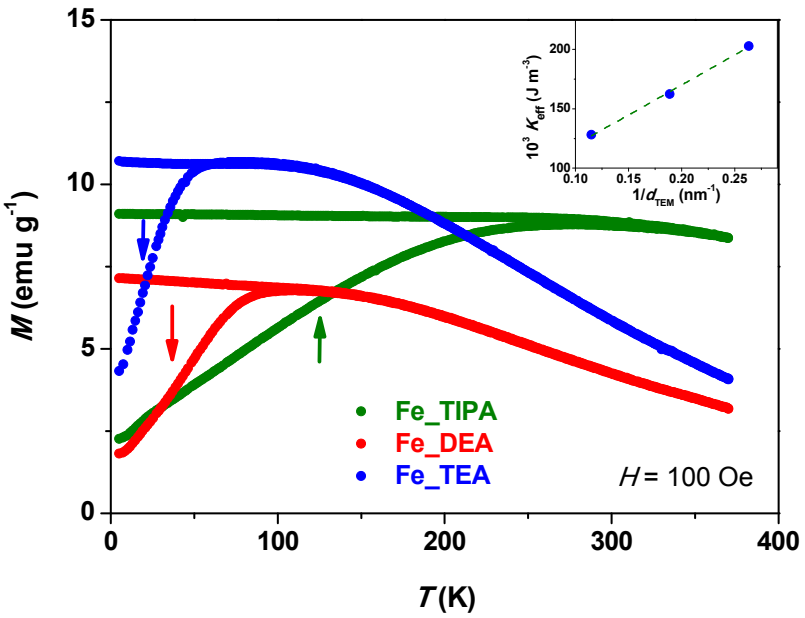

Figure 6

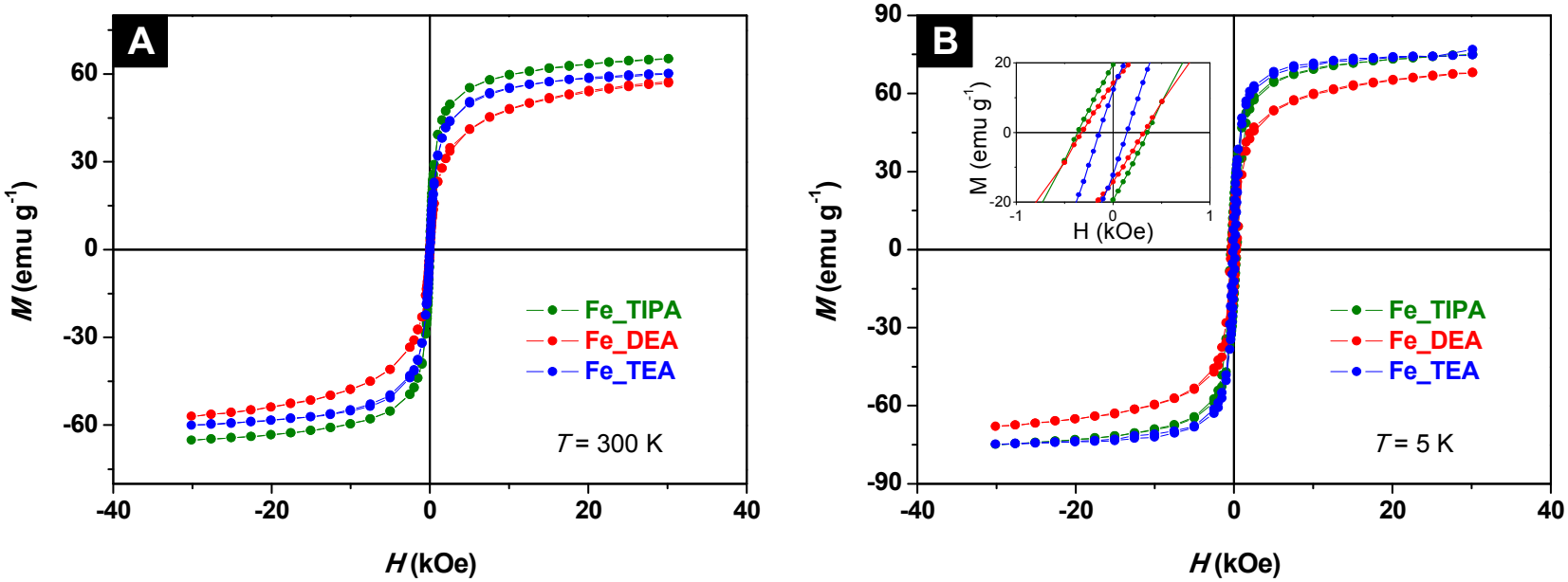

Figure 7

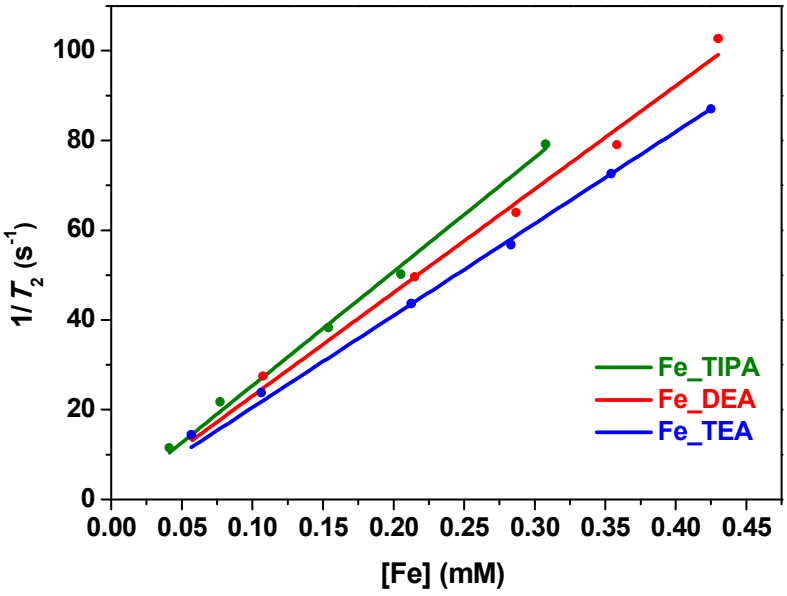

Figure 8

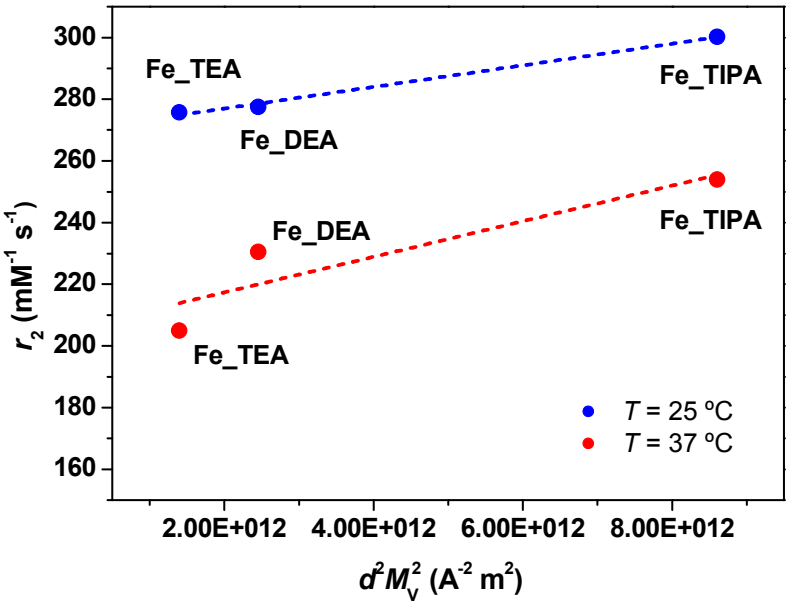

Figure 9